Supplementary Information (SI) for ChemComm.
This journal is © The Royal Society of Chemistry 2026

Supplementary Information

Symmetrical Waveform Alternating Current Driven Electron Enrichment for Enhanced Oxygen Evolution Reaction

Jinhui hao*, Zhenghao Zhang, Yitian Wu, Xiao Yang, Qianwen Qiu, Wenshu Yang, Longhua Li, Weidong Shi*

Experimental section

Materials

$Ni(NO_3)_2$, $Fe(NO_3)_3$, carbon paper and KOH were purchased from Sinopharm Chemical Reagent Co., Ltd. The solution purity is AR grade. All chemicals were used without further purification.

Synthesis of $NiFeO_xH_y$

A 2 cm × 2.5 cm carbon paper was ultrasonically treated in ethanol and deionized water respectively for 20 minutes. 15 ml of 0.5 M $Ni(NO_3)_2$ solution and 15 ml of 0.5 M $Fe(NO_3)_3$ were added to the electrolytic bath, with Ag/AgCl, carbon paper, and Pt used as the reference electrode, working electrode, and counter electrode respectively. Electrodeposition was carried out at an applied potential of -1.5 V for 100 seconds. The carbon paper was rinsed with deionized water and dried to obtain the precursor. The precursor was placed in a tube furnace and heated to 400 °C at a ramp rate of 10 °C/min in an atmosphere of air and kept at this temperature for 120 minutes and then cooled to room temperature to obtain the $NiFeO_x$ catalyst. Using $NiFeO_x$ as the initial electrocatalyst, $NiFeO_x$ was pre-scanned by LSV technique until the current density response stabilized. This process led to the full oxidation of the surface structure of the electrocatalyst, and the obtained electrocatalyst was noted as $NiFeO_xH_y$.

Synthesis of NiOxHy-AC-X

The SWAC treatment was conducted in a three-electrode system, where Hg/HgO, NiFeOxHy, and glassy carbon served as the reference electrode, working electrode, and counter electrode, respectively. During the SWAC process, a symmetric sinusoidal waveform with a frequency of 2 Hz was employed. Each potential step was maintained for 5 seconds, with each cycle lasting 80 seconds. Fifteen such cycles were conducted, totaling 20 minutes of processing time during which 120 AC potential cycles were performed.

Characterization

X-ray diffraction (XRD) was employed to analyze the crystalline structure of the samples. The diffractometer model used was the SmartLab9 manufactured by Rigaku

Corporation, Japan. The diffraction source was Cu Kα (1.5406 Å), with a tube voltage of 40 kV and a current of 40 mA. The measurement range was 10–80°, and the scanning speed was 10°/min. Scanning electron microscopy (SEM) was used to examine the surface microstructure of the samples. The instrument used was a Hitachi S-4800 model. Samples were washed with water, dried, mounted on the specimen stage, and imaged in selected regions. X-ray Photoelectron Spectroscopy (XPS) analysis was performed on an Escalab 250Xi X-ray spectrometer manufactured by Thermo Fisher Scientific, USA, mainly to characterize the chemical elemental composition and valence states of the samples. Electron Paramagnetic Resonance (EPR) was used to analyze the state of unpaired electrons within the catalyst and the structural characteristics of its surrounding environment. The instrument model used in this study was the A300-10/12. In situ Raman spectroscopy was performed during electrochemical control to monitor structural changes of the $NiFeO_xH_y$ surface. Spectra were acquired at potentiostatic steps of 1.2, 1.4, and 1.6 V vs RHE in 1.0 M KOH at 30 °C. Measurements used a 532 nm excitation, laser power at the sample ≤ 1 mW, spectral resolution ≈ 1 cm−1, single-spectrum accumulation time 60 s with 3 accumulations averaged per spectrum, and standard spectral calibration procedures with a silicon reference. The operando cell employed a three-electrode configuration with the SWAC-treated $NiFeO_xH_y$ on carbon paper as the working electrode, a Pt counter electrode, and a Hg/HgO reference electrode (all potentials converted to RHE).

Electrochemical measurements

All electrochemical measurements were conducted using a three-electrode system. The prepared catalyst was directly used as the working electrode, glassy carbon as the counter electrode, and a mercury/mercury oxide electrode as the reference electrode. The electrolyte used was 1 M KOH, and the electrochemical measurements were performed on a CHI660e electrochemical workstation. The alkaline membrane used in the tests had a thickness of 183 μm and a conductivity of 0.083 S/cm.

Computational data for E_{app} and DRT

E_{app} was obtained from Arrhenius plots using reaction rates measured at five temperatures (25, 35, 45, 55, 65 °C); for each applied overpotential we extracted the

steady-state rate constant from potentiostatic i–t data, plotted ln(k) versus 1/T, and determined E_{app} from the slope of a linear fit; a lower E_{app} is thus interpreted as a reduced effective kinetic barrier under the specified electrochemical conditions. For DRT, raw EIS spectra (frequency range 100 kHz - 0.1 Hz, 10 points/decade, AC amplitude 5 mV RMS) were baseline-corrected before DRT deconvolution. The integrated areas and peak positions (with estimated uncertainties) are reported to quantify changes in high-frequency interfacial/mass-transport contributions and lower-frequency charge-transfer/adsorbate kinetics after SWAC activation.

Computational details of the DFT model

The electronic properties of the catalysts were investigated by DFT calculations using the VASP code[1]. DFT calculations were performed with periodic slab models using the PBE exchange–correlation functional with, a plane-wave cutoff of 500 eV. Surface models used 2 × 2 in-plane supercells, a 15 Å vacuum gap normal to the slab, and a Monkhorst–Pack k-point mesh of 3 × 3 × 1 (denser meshes used for selected PDOS calculations as noted in the Supplement). Electronic self-consistency was converged to 1×10^{-5} eV and ionic relaxations to forces below 0.01 eV $Å^{-1}$. For the DFT calculations, oxygen vacancies were introduced at symmetry-equivalent positions to ensure structural stability and represent a reasonable defect configuration. The vacancy concentration was set according to the XPS-derived ratio (2:3).

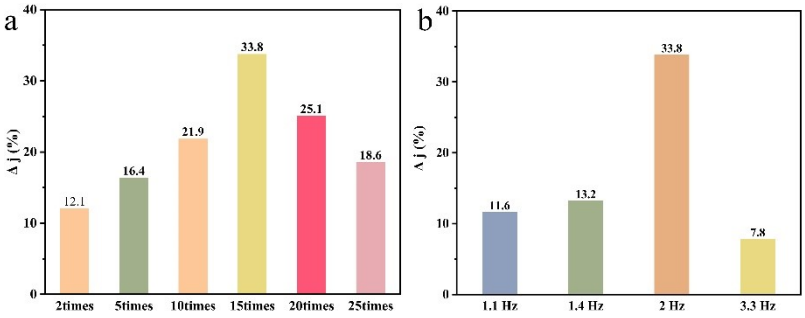

Fig. S1 (a) Relative change in current density as a function of SWAC treatment duration. (b) Relative change in current density as a function of applied SWAC frequency.

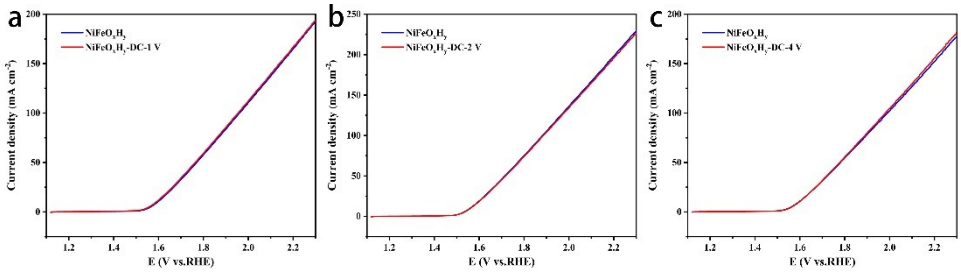

Fig. S2 Effect of DC activation forward potential on LSV performance. (a) $NiFeO_xH_y$-DC-1V. (b) $NiFeO_xH_y$-DC-2V. (c) $NiFeO_xH_y$-DC-4V.

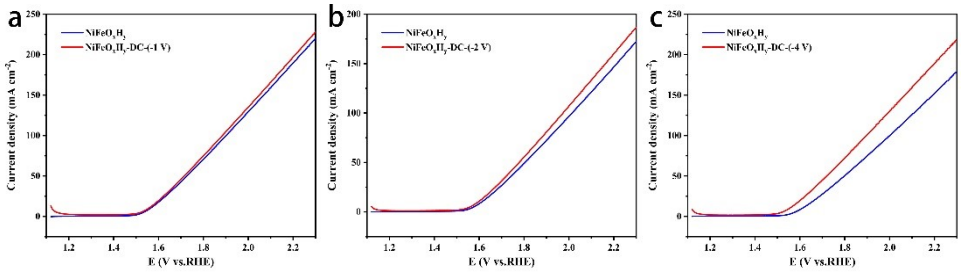

Fig. S3 Effect of DC activation reverse potential on LSV performance. (a) $NiFeO_xH_y$-DC-(-1V). (b) $NiFeO_xH_y$-DC-(-2V). (c) $NiFeO_xH_y$-DC-(-4V).

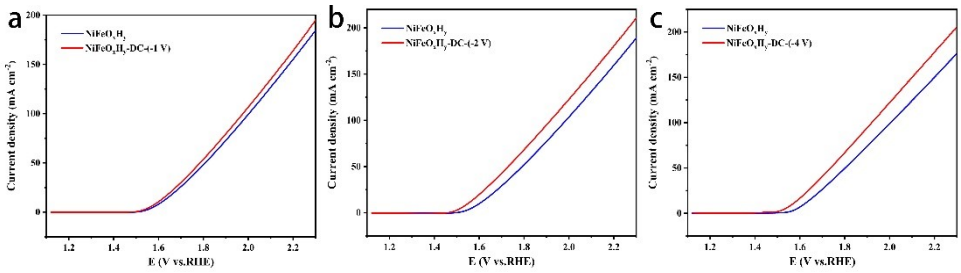

Fig. S4 Backscan LSV curves of $NiFeO_xH_y$-DC-(-1V) (a), $NiFeO_xH_y$-DC-(-2V) (b), and $NiFeO_xH_y$-DC-(-4V) (c).

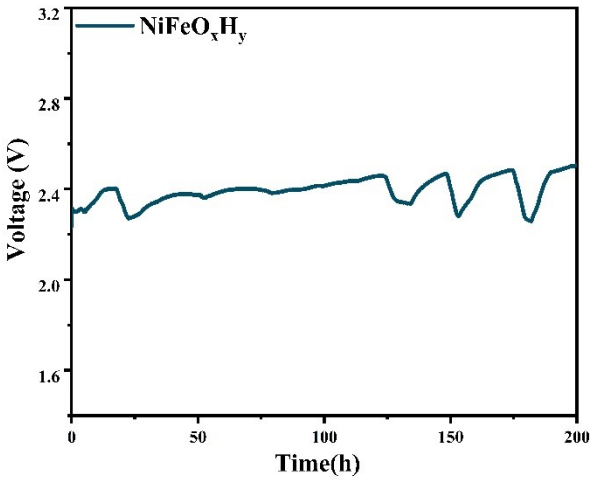

Fig. S5 Stability testing of $NiFeO_xH_y$ at a current density of 200 mA cm^{-2}.

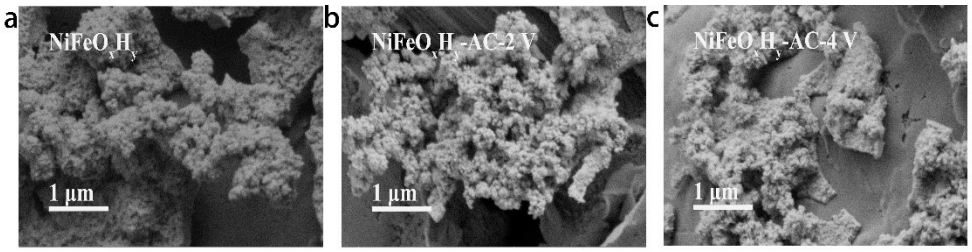

Fig. S6 SEM images of $NiFeO_xH_y$ and $NiFeO_xH_y$-AC-X. (a) $NiFeO_xH_y$. (b) $NiFeO_xH_y$-AC-2V. (c) $NiFeO_xH_y$-AC-4V.

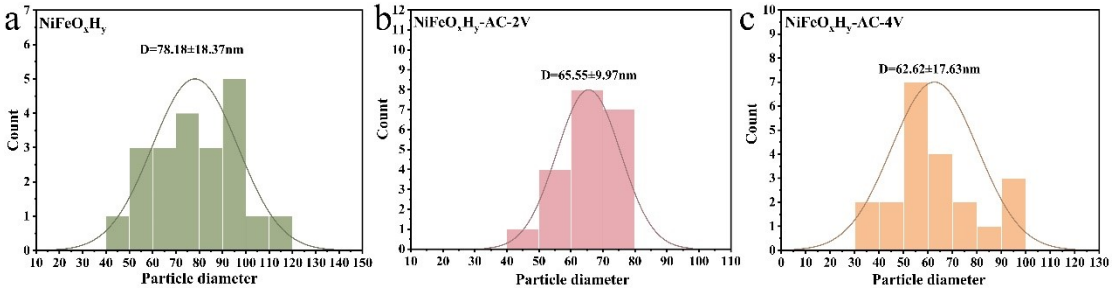

Fig. S7 The average particle diameter of the catalyst. (a) $NiFeO_xH_y$. (b) $NiFeO_xH_y$-AC-2V. (c) $NiFeO_xH_y$-AC-4V.

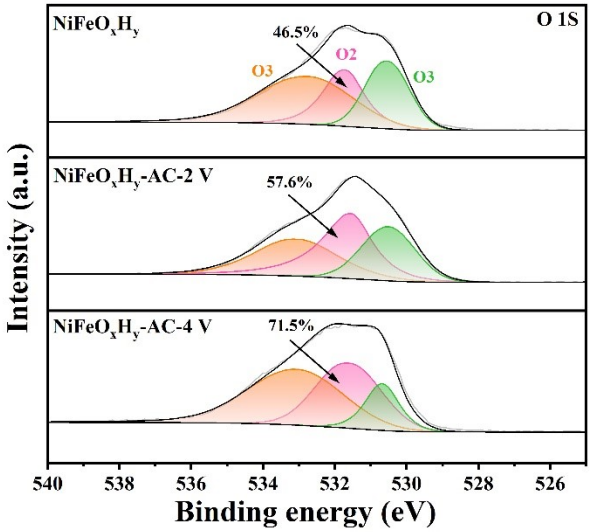

Fig. S8 O 1s XPS spectra of $NiFeO_xH_y$ and $NiFeO_xH_y$-AC-X.

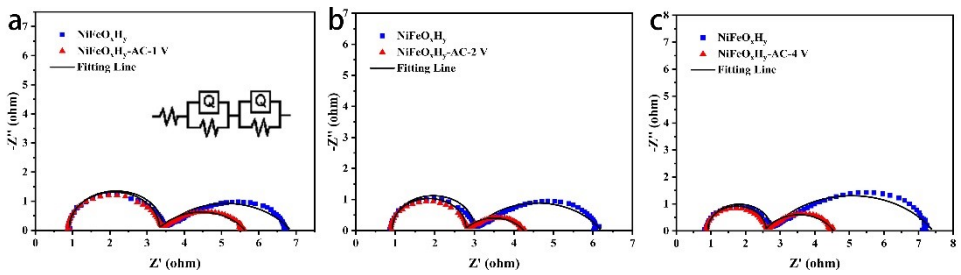

Fig. S9 EIS (R_{ct}) plots of $NiFeO_xH_y$ and NiFeOxHy-AC-X. (a) $NiFeO_xH_y$ -AC-1V. (b) $NiFeO_xH_y$ -AC-2V. (c) $NiFeO_xH_y$ -AC-4V.

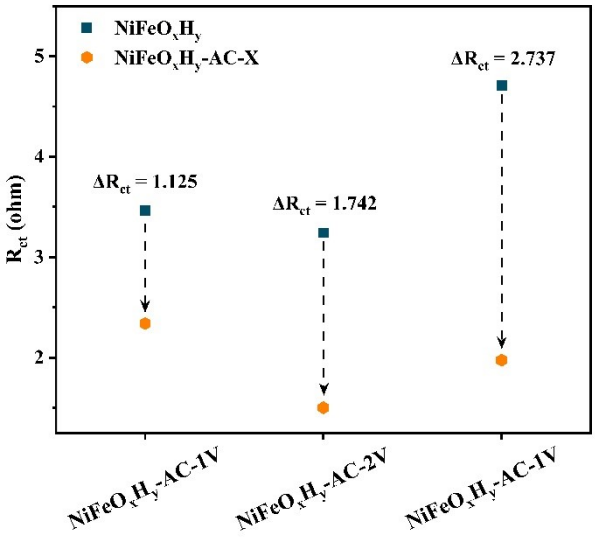

Fig. S10 R_{ct} variation for $NiFeO_xH_y$ and $NiFeO_xH_y$-AC-X.

.

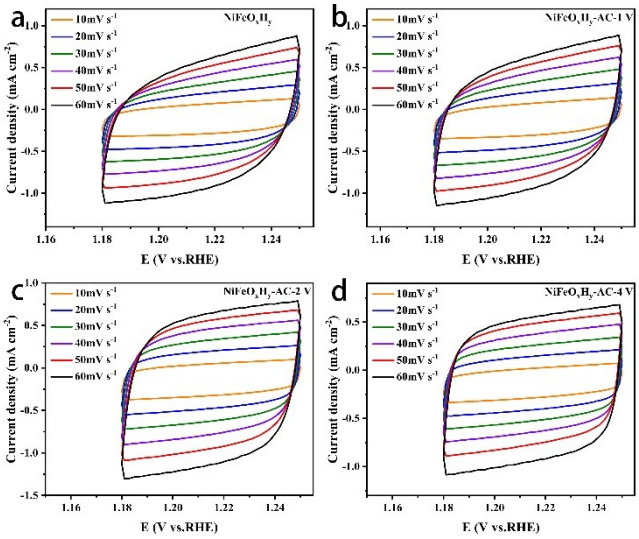

Fig. S11 CV curves of $NiFeO_xH_y$ and $NiFeO_xH_y$-AC-X. (a) $NiFeO_xH_y$. (b) $NiFeO_xH_y$-AC-1V. (c) $NiFeO_xH_y$-AC-2V. (d) $NiFeO_xH_y$-AC-4V.

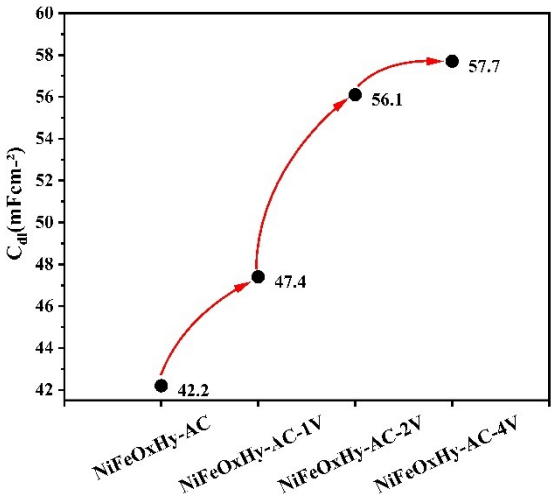

Fig. S12 C_{dl} of $NiFeO_xH_y$-AC-X and $NiFeO_xH_y$-AC-X.

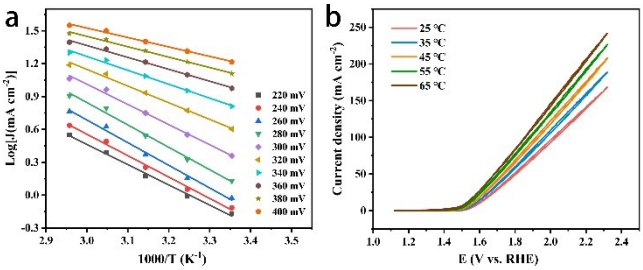

Fig.S13 (a) Plot in Log(j) for 1000/T. (b) CV curves of $NiFeO_xH_y$ at different temperatures.

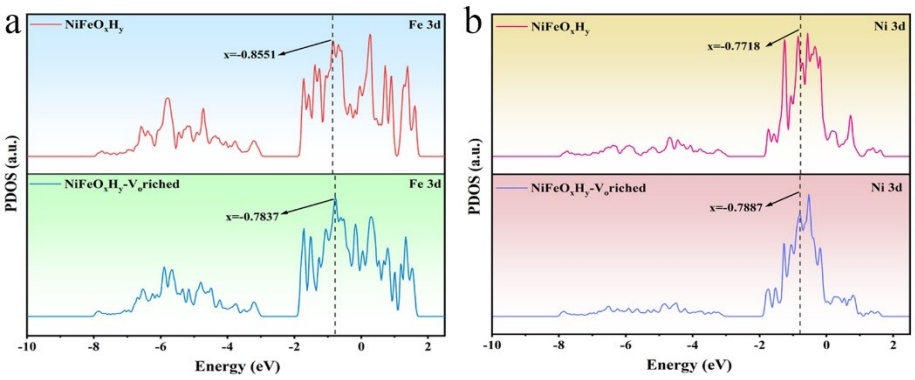

Fig.S14 (a) PDOS diagram of Fe 3d. (b) PDOS diagram of Ni 3d.

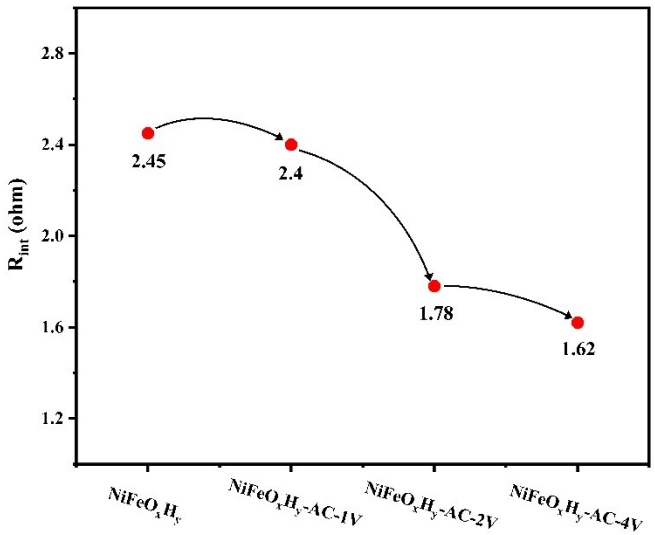

Fig.S15 Changes in internal resistance before and after SWAC activation.

Table.S1 Comparison of different activation strategies and performance of NiFe-Based Catalysts.

Catalyst	Reduced in overpotential (mV)/mA cm^{-2}	Performance variation	Activation Method	Ref.
A-NiFe-TDC-5	54/j_{10}	↓ 2.7%/450h	Cathodic activation	[2]
g-C_3N_4@S/NiFe-LDH-3	110/j_{50}	↓ 7.8%/100h	Cathodic activation	[3]
cd-NiFe LDH-$NaBH_4$	65/j_{10}	/	$NaBH_4$ activation	[4]
F-NiFe-A	32/j_{10}	/	Electrochemically Reconstruction	[5]
Ir/NiFe LDH	78/j_{100}	↓ 1.7%/200h	Electrostatic adsorption strategy	[6]
O_v-NiFe-LDH/$Ti_3C_2T_x$/NF	122/j_{100}	↓ 2.4%/20h	Plasma discharge engineering	[7]
$NiFeO_xH_y$-AC-4V	60/j_{10} 92/j_{50} 132/j_{100}	Stable/200h	SWAC	This work

Table.S2 The relative abundance of Ni^{3+}, Fe^{3+} and V_o.

Catalyst	$Ni^{3+}/Ni^{3+}+Ni^{2+}$	$Fe^{3+}/Fe^{3+}+Fe^{2+}$	V_o
$NiFeO_xH_y$	41.1%	31.3%	46.5%
$NiFeO_xH_y$-AC-2V	51.5%	40.3%	57.6%
$NiFeO_xH_y$-AC-4V	52.3%	52.3%	71.5%

Table.S3 EIS fitting data for $NiFeO_xH_y$ before and after symmetric waveform AC activation at different potentials.

		R_1 (Ω)	R_{int} (Ω)	CPE_1-T (10^{-7} $F^{-1}\cdot s^{1-n}$)	CPE_1-P	R_{ct} (Ω)	CPE_2-T ($F^{-1}\cdot s^{1-n}$)	CPE_2-P
Sample 1	$NiFeO_xH_y$	0.926	2.466	6.665	1.56	3.463	0.033	0.624
	$NiFeO_xH_y$-AC-1V	0.918	2.373	6.113	1.062	2.338	0.031	0.627
Sample 2	$NiFeO_xH_y$	0.932	2.039	7.728	1.061	3.242	0.039	0.638
	$NiFeO_xH_y$-AC-2V	0.939	1.813	6.105	1.081	1.5	0.038	0.629
Sample 3	$NiFeO_xH_y$	0.903	1.805	9.069	1.054	4.684	0.023	0.644
	$NiFeO_xH_y$-AC-4V	0.917	1.646	7.748	1.068	1.947	0.025	0.696

References

1 K. Dang，J. Chen，B. Rodgers and S. Fensin,Computer Physics Communications,2023,286,108667.

2 B.-C. Shi，M. Jin，Y. Zou，S. Wang，Y. Nie，D. Yao and Y.-J. Tang,Rare Metals,2025,10.1007/s12598-12025-03446-12590.

3 Y. Cui，C. Wu，J. Wu，H. Hu，M. Ling，X. Gao and C. Liang,Sustainable Materials and Technologies,2025,44,e01367.

4 X. Li，Y. Liu，Q. Sun，Z. Huangfu，W.-H. Huang，Z. Wang，C.-C. Chueh，C.-L. Chen and Z. Zhu,ACS Sustainable Chemistry & Engineering,2022,10,14474-14485.

5 Q. Xu，H. Jiang，X. Duan，Z. Jiang，Y. Hu，S. W. Boettcher，W. Zhang，S. Guo and C. Li,Nano Letters,2020,21,492-499.

6 D. Li，L. Ding，S. Zhang，P. Zhang，C. Prestigiacomo，D. Wang and Q. Zhao,Chemical Engineering Journal,2025,519,165662.

7 S. Peng，H. Yu，Y. Wen and W. Peng,Ionics,2025,31,7155-7168.